Multiple Extended Target Tracking for Through Wall Radars

Gianluca Gennarelli, Gemine Vivone, Paolo Braca, *Member, IEEE,* Francesco Soldovieri, *Senior Member, IEEE*, and Moeness G. Amin, *Fellow, IEEE*

***Abstract*—Tracking moving targets hidden behind visually opaque structures as building walls is a crucial issue in many surveillance, rescue, and security applications. The electromagnetic waves at low microwave frequency range penetrate into common building materials and thereby enable the radar to expose behind the wall scene. However, due to complexity of the scattering scenario, the radar signal undergoes multipath propagation phenomena. These typically manifest themselves as environmental clutter which may impair detection and tracking of true targets. In this paper, a signal processing strategy is proposed to track multiple *extended* targets in a scene by means of a wide-band monostatic through wall radar. The system collects datasets at regular time steps which are firstly processed by a microwave tomographic technique. Then, a detection/tracking stage is implemented in order to track the position and dynamics of targets in real-time. An extended target tracking approach is applied to properly exploit at the tracking stage the information related to extended nature of targets. The effectiveness of the proposed signal processing chain is assessed by numerical tests based on full-wave data pertaining to an indoor scenario.**

***Index Terms*—extended target tracking, microwave tomography, through wall radar.**

I. Introduction

THROUGH wall radars (TWRs) are valuable diagnostic devices in civilian and military areas owing to their applicability in homeland security (e.g. counter terrorism and urban warfare), search and rescue missions in natural disaster, crisis scenarios management, etc. [1], [2]. A TWR emits a wide-band electromagnetic (EM) pulse with frequency content ranging from some hundreds MHz to few GHz. As common building materials are penetrable at those frequencies, targets behind the wall scatter back to the radar part of the incident EM energy and are therefore detectable.

A major problem encountered when processing TWR signals is the ringing effect caused by multiple reflections inside the front wall, which represent the stronger clutter source when imaging stationary targets. Some common approaches to mitigate front wall reflections are the background removal [2], the spatial filtering [3], and subspace wall projections [4].

G. Gennarelli and F. Soldovieri are with the Institute for Electromagnetic Sensing of the Environment, National Research Council of Italy, Via Diocleziano 328, 80124, Napoli, Italy. E-mail: gennarelli.g,soldovieri.f@irea.cnr.it.

G. Vivone and P. Braca are with the North Atlantic Treaty Organization (NATO) Science and Technology Organization (STO) Centre for Maritime Research and Experimentation, 19126 La Spezia, Italy. E-mail: gemine.vivone,paolo.braca@cmre.nato.int.

M. G. Amin is with the Center for Advanced Communications, Villanova University, Villanova, PA 19085 USA. E-mail: moeness.amin@villanova.edu.

Aside from techniques to mitigate clutter, a great deal of work has been done in the field of Through Wall Radar Imaging (TWRI). TWRI algorithms aim at providing to the end-user an image of the surveillance area more easily interpretable with respect to raw data. Examples include the delay and sum beamforming [5], the time-reversal multiple signal classification method [6], and methods lying within the framework of EM inverse scattering. These include the non-linear tomographic approach [7], and the linear inverse scattering techniques based on the diffraction tomography [8] and on the singular value decomposition (SVD) [9], [10]. The aforementioned techniques have been applied to detect targets located behind homogenous slab walls, and their effectiveness has been experimentally assessed (e.g. see [8], [9], [11]). More sophisticated imaging schemes have been also devised for complex multiscattering environments, such as inhomogeneous cinderblock walls [12], enclosed rooms [13], and building corners [14]. Accurate modeling of the EM scattering phenomenon is a necessary requirement to obtain images free from artifacts and distortions. Most notably, multipath signals can be effectively exploited to improve the imaging performance [15], [16].

The image formation process represents the preliminary step before performing higher level signal processing tasks. These include automatic target detection [17], [18], which represents a fundamental step to follow-on stages such as classification [19], [20] and tracking [21]–[23].

In this paper, we address the problem of tracking multiple moving targets in TW scenarios. The problem has not received the proper attention and only few studies have been reported to date [21]–[23]. Indeed, the identification of moving targets has been mostly achieved via change detection schemes [24]–[27]. Change detection provides an indication of moving targets by suppressing stationary clutter by applying coherent or non-coherent subtraction among data frames. In view of its relative simplicity and effectiveness in getting situation awareness in practical scenarios, change detection has appeared to be the preferred approach for indoor target detection. However, apart from surveillance of human activities in a typical household, real-time tracking of criminals and adversaries on the move could be required and carried out by law enforcement officers. In this case, target identification, position, and speed need to be continuously provided via a tracking algorithm.

Radar target tracking is a complex process which, besides suppression of static clutter, involves the joint detection and estimation of a time-varying and unknown number of targets [28]. A target tracking procedure consists of the following

three steps. The data association step tries to filter out spurious contacts (false alarms) and links each measurement to the corresponding target. The track management step determines which tracks need to be generated or deleted. The filtering step reduces the effects of measurement errors and nonlinearities providing an estimate of the target state.

The available tracking procedures for TWRs rely on the time-of-arrival estimation for target detection and implement the common Kalman filter (KF) (e.g. see [21]–[23]). KF assumes that one detection measurement per target is *always* available for each frame without any ambiguity in the data association. This assumption is not realistic since TWRs suffer from false alarm and target miss detection. Application of modern multi-target tracking techniques are, therefore, necessary to deal with the data association problem and to provide operationally acceptable performance.

In recent years, many approaches and paradigms have emerged in target tracking literature [28], [29], including multiple hypotheses tracking (MHT) [28], the joint probabilistic data association (JPDA) rule [28], [30], sequential Monte Carlo methods (SMC) [31]–[33], and the probability hypothesis density (PHD) filter [29], [34], [35].

An important aspect of moving targets inside enclosed structures is the spatial extent over contiguous range cells. In essence, humans are extended targets imaged as spots (i.e. groups of pixels) that generate a cloud of detections.

Extended target tracking (ETT) is a procedure which provides an estimation of position and dynamics of targets but also of their sizes. This additional information can be effectively utilized to improve the data association and, in turn, enhance the system performance [36]. ETT has been introduced in marine radar [37], [38], video surveillance [39], laser range [40], etc., based on different methodologies such as random matrices filtering [41], probability hypothesis density (PHD) [38], [40] and track-before-detect (TbD) [37], [42].

In this work, we present a strategy for processing the signals collected by a wide-band monostatic TWR. The first stage involves a pre-processing of raw data and the image formation process, which is performed by a microwave tomographic approach. In the second stage, each image is given as input to an object detector, constituted by a constant false alarm rate (CFAR) detector [43] and by a clustering procedure. The CFAR is properly exploited to account for the extended nature of the targets. The detected objects are then processed according to the JPDA rule. It is worth noting that the JPDA has lower performance than the MHT and the PHD but has a lower complexity, comparable to the simple Kalman filter. This aspect is crucial to ensure a real-time operation of the tracking procedure for the typical frame rates of TWRs. Numerical experiments based on full-wave data pertaining to an indoor scenario were performed to test the effectiveness of the signal processing chain. The tracking stage improves considerably the performance with respect to the stand-alone detector.

The paper is organized as follows. Section II deals with the radar imaging approach. Section III addresses the target detection, while Sec. IV is focused on the ETT procedure. Numerical results are reported in Sec. V and conclusions are made in Sec. VI.

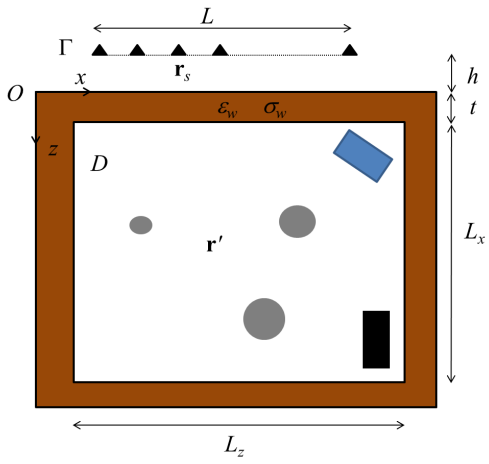

Fig. 1. Sketch of the TW scenario. Multiple moving targets (circles) and static objects (rectangles) are located inside an enclosed room and probed by a wide-band monostatic TW radar.

II. TWRI APPROACH

We consider the two-dimensional (2D) scenario shown in Fig. 1. A group of moving targets (circles) is present in the surveillance region D together with static objects (rectangles). The walls surrounding D are homogeneous non-magnetic dielectric slabs characterized by the relative permittivity ϵ_w and electric conductivity σ_w. The scene is illuminated by an array of antennas covering the line Γ with length L and placed at a stand-off distance h from the visible front-wall interface ($z = 0$). Each element in the array emits a wide-band electromagnetic pulse with frequency content in the band $B = [f_{min}, f_{max}]$ and collects the radar echo. As a result, a multimonostatic/multifrequency configuration is adopted. The radiating elements are modeled as electric line currents polarized along the y-axis. Let $\boldsymbol{r}_s = x_s\hat{x} - h\hat{z}$ denote the position of each antenna along Γ, while $\boldsymbol{r}' = x'\hat{x} + z'\hat{z}$ is the position of a generic point in D. An $\exp(i2\pi f t_f)$ time dependence is assumed and suppressed, being t_f the fast-time spanning the window $[0, T_{ft}]$.

We assume the array to be a physical aperture where each antenna is electronically switched on and off recording the total field signal $E_{tot}(\boldsymbol{r}_s, t_f)$. This operation is repeated periodically at times $t_s = k\Delta$, $k = 1, ..., K$, with Δ being the the time step between two consecutive frames and K representing the total number of frames recorded over the slow-time interval $[0, T_{st}]$. From this point on, the index k is adopted to denote the frame at slow-time $t_s = k\Delta$.

A pre-processing based on a time-gating is applied to the entire dataset to filter out the direct coupling signal and the front wall response. The resulting data are then transformed into the frequency domain, providing the scattered field dataset $E_s(\boldsymbol{r}_s, f, k)$, $k = 1, ..., K$.

The following analysis is focused on perfectly conducting targets. Let τ_p be the contour of object p and $\tau = \bigcup_{p=1}^{P} \tau_p$ is the union of all contours, with P being the total number of targets. The TWRI goal is to retrieve τ from the electric field E_s scattered by the targets in the scene. For the 2D case at hand, the problem is scalar and the scattered field originated by

the electric currents J induced on the unknown target contours is expressed by the integral relationship [44]:

$$E_s(\boldsymbol{r}_s, f, k) = -j2\pi f\mu_0 \int_\tau G(\boldsymbol{r}_s, \boldsymbol{r}', f) J(\boldsymbol{r}_s, \boldsymbol{r}', f, k)\, d\tau \tag{1}$$

where $G(\boldsymbol{r}_s, \boldsymbol{r}', f)$ is the Green's function relevant to the background scenario, and μ_0 is the magnetic permeability of free-space.

The inverse problem defined by eq. (1) is non-linear because of mutual interactions between targets and different parts of the same target. From a mathematical perspective, this implies that the unknown current distribution J depends not only on the incident field but also on the unknown τ.

In view of the computational complexity and convergence issues related to non-linear inversion methods [7], a typical strategy is to resort to simplified linearized models of the scattering phenomenon. Under physical optics approximation (PO), holding for targets with smooth contours and large (in terms of wavelength) radii of curvature, eq. (1) can be rewritten as a linear integral equation [45]:

$$\begin{aligned} E_s(\boldsymbol{r}_s, f, k) \quad &= -j2\pi f\mu_0 \times \\ &\int_D G(\boldsymbol{r}_s, \boldsymbol{r}', f) E_i(\boldsymbol{r}_s, \boldsymbol{r}', f)\gamma(\boldsymbol{r}', k) d\tau \end{aligned} \tag{2}$$

in which E_i is the incident field in D and γ is an unknown complex value distribution supported over τ. Accounting for the effect of clutter and noise, eq. (2) can be rewritten as

$$E_s = L\gamma + \nu \tag{3}$$

where $L : U \rightarrow V$ is a linear projector operator and ν is a clutter/noise term. U and V are assumed Hilbert spaces of square integrable functions.

The above equation must be inverted with respect to the unknown γ, i.e. a linear inverse problem must be solved. To this end, the kernel of the operator L (i.e. E_i and G) must be evaluated. With regard to the scenario depicted in Fig. 1, the background Green's function is not available in closed form and may be computed numerically [46]. This operation requires the knowledge of the room layout which could be not available and should then be estimated. To overcome this difficulty, E_i and G are calculated by accounting only for wave propagation through the infinite dielectric slab modeling the front wall [9], [47]. Such an approximation is reasonable since multipath echoes associated with reflections inside the room have generally lower amplitude than direct scattering returns. The front wall geometrical and electrical properties (ϵ_w, σ_w and t) are assumed known or accurately estimated [8], [10].

The linear inverse problem defined by eq. (3) is ill-posed [48]. Since real data are affected by clutter and noise, they may not belong to the range of L and the existence of the solution is not ensured. Accordingly, a generalized solution is typically searched for by minimizing a cost functional accounting for the distance in the data space between the measured scattered field and the one predicted by the scattering model, i.e.

$$\tilde{\gamma} = \inf_{\gamma}(\|E_s - L\gamma\|^2) \tag{4}$$

Since the operator L is compact, the solution to the problem (4) does not depend continuously on data and regularization is required to retrieve a stable solution. The strategy then adopted is based on the adjoint operator $L^\dagger$, i.e.

$$\tilde{\gamma} = L^\dagger E_s \tag{5}$$

which is equivalent to a migration scheme [16]. The regularized solution defined by eq. (5) is a good approximation of the solution to eq. (4) provided that the singular values of the operator have a step-like behavior [48]. If this condition is not met, a poorer resolution is typically achieved in final images. However, the adjoint inversion scheme is preferred here due to its lower computation effort, which is an essential advantage in view of the real-time processing constraint.

From this point on, the spatial map $I(\boldsymbol{r}, k)$ defined by the amplitude of $\tilde{\gamma}$ normalized to its maximum is referred as tomographic image.

III. Object detection

The standard approach to the tracking target problem is divided in two main parts: i) detection and ii) tracking [28].

An overview of the overall signal processing chain is depicted in Fig. 2. As can be noticed, the detector receives, as inputs, the TWR images obtained by adjoint inversion. The order statistic CFAR (OS-CFAR) detector introduced in [43] is considered in the processing chain.

CFAR detectors estimate the clutter/noise power by adapting the threshold to maintain a desired probability of false alarm P_{FA}. The square amplitude of each pixel in the image (cell under test) is compared to a threshold depending on the estimated noise power and P_{FA}. The noise power is evaluated by considering the cells in a reference window. A guard window is used to exclude cells immediately adjacent to the cell under test since they contain both clutter/noise and target energy.

In OS-CFAR detection, the observations in the reference window are sorted to form a sequence in ascending numerical order $\{I_{(1)}, I_{(2)}, \ldots I_{(N_c)}\}$, with N_c being the number of cells in the reference window. The q^{th} order statistic $I_{(q)}$ is chosen as representative of the interference level, and the threshold is set as a multiple of this value

$$Th = \alpha I_{(q)}. \tag{6}$$

For a square-law detector assuming *independent identically distributed* (i.i.d.) Gaussian interference in the in-phase (I) and quadrature-phase (Q) signals (i.e. the interference is exponential distributed), the constant α is related to P_{FA} as [43]

$$P_{FA} = q\frac{N_c!}{q!\,(N_c - q)!}\frac{(q-1)!(\alpha + N_c - q)!}{(\alpha + N_c)!}. \tag{7}$$

As suggested in [43], the 75^{th} percentile (i.e. $I_{(0.75N_c)}$) is selected to evaluate Th.

The output of the OS-CFAR detector at a given time scan k is represented by the detections, defined by $\mathcal{Y}_k = \{\boldsymbol{y}_{1,k}, \boldsymbol{y}_{2,k}, \ldots, \boldsymbol{y}_{n_k,k}\}$, where $\boldsymbol{y}_{i,k} \in D$ is the position of the i^{th} detection, and n_k is the total number of detections that may vary over k.

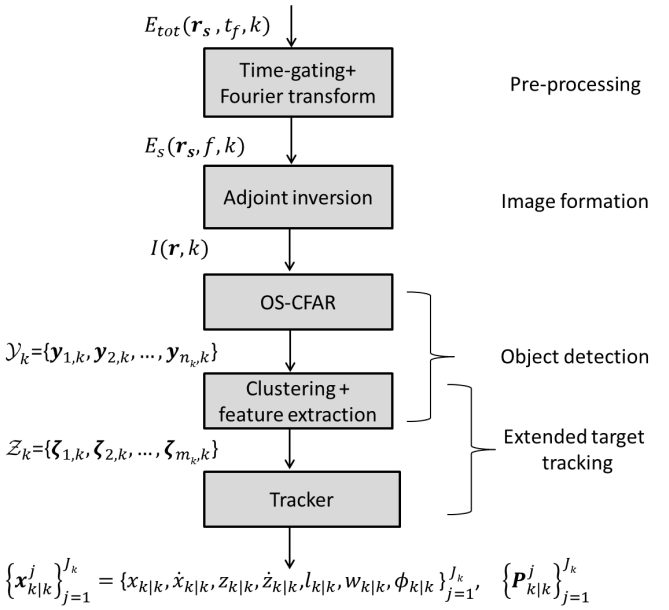

Fig. 2. Block diagram of the TWR signal processing chain. The raw data $E_{tot}\left(\boldsymbol{r}_s, t_f, k\right)$ are time-gated and transformed into frequency domain. The frequency domain scattered field data $E_s\left(\boldsymbol{r}_s, f, k\right)$ are processed by adjoint inversion to get the tomographic image. The object detection based on OS-CFAR, clustering, feature extraction provides the set of measurements $\mathcal{Z}_k$ required for the tracking. The tracker output is the state estimate $\left\{\boldsymbol{x}_{k|k}^j\right\}_{j=1}^{J_k}$ and the covariance matrix $\left\{\mathbf{P}_{k|k}^j\right\}_{j=1}^{J_k}$, where J_k is the number of active tracks at time k.

Starting from the set of detections $\mathcal{Y}_k$, a clustering is carried out to group the detections that are likely to be generated by the same targets. The clustering procedure exploits the group connectivity of detections, i.e. the spatial relation of a detection with its neighbors. A detection is said "8-connected" if all detections belonging to its 8-neighborhood (i.e. the adjacent detections in vertical, horizontal, and diagonal directions) can be considered part of the cluster.

As a general and simple model for the target extent, we exploit the common ellipsoidal representation, e.g. see [37], [41], [49], [50]. In many real-life target tracking scenarios, the targets are neither sufficiently far from the sensors to generate only a single measurement, nor are they sufficiently close to the sensors such that their features are clearly articulated [50]. This consideration mainly justifies the model hypothesis for the targets' extents. Afterwards, starting from the clusters, the parameters that fully characterize the elliptical model are estimated. The estimation is carried out using the normalized second central moments [51]. After this stage, a new set of measurements $\mathcal{Z}_k = \{\boldsymbol{\zeta}_{1,k}, \boldsymbol{\zeta}_{2,k}, \ldots, \boldsymbol{\zeta}_{m_k,k}\}$ is obtained where m_k is the total number of detected objects at time k. In greater details, the generic entry $\boldsymbol{\zeta}_{i,k} = \left[\boldsymbol{\zeta}_{i,k}^{(p)}, \boldsymbol{\zeta}_{i,k}^{(s)}, \zeta_{i,k}^{(\phi)}\right]^{\mathrm{T}}$ contains the estimated parameters of the ellipse that fits the i^{th} object. Hence, $\boldsymbol{\zeta}_{i,k}^{(p)} \in D$ is the position of the center of the object, $\boldsymbol{\zeta}_{i,k}^{(s)} \in \mathbb{R}^2$ is the object size constituted by the major and minor ellipse axes, and $\zeta_{i,k}^{(\phi)}$ is the object orientation with respect to the x-axis.

It is worthwhile to note that in some ETT approaches the ellipse parameter estimation is implicitly carried out during the filtering, e.g. see [37], [38], [41], [42]. In this work, we prefer to strictly separate tracking from the other phases with the aim of exploiting well-established target tracking approaches [28]. The main advantages can be found in the usually low computations in the multi-target case ensuring real-time executions. Thus, the multi-target tracking algorithm, detailed in the next section, is fed by $\mathcal{Z}_k$ for each time k to get its outcomes.

IV. ETT PROCEDURE BASED ON JOINT PROBABILISTIC DATA ASSOCIATION

The extended target tracking (ETT) procedure based on the joint probabilistic data association (JPDA) algorithm is exploited in this paper [28], [30]. Firstly, a description of both motion and measurement models adopted to track the objects synthesized by the means of the features extracted in the previous step is provided. Then, the ETT algorithm is described in detail. The track management process can be divided into track initiation, track update, and track elimination. The track update is performed based on both the data association, which determines how detections (clutter- and target-originated measurements) are associated to the existing tracks, and the track filtering step, which includes the target motion model used to predict and update the target state of the tracks.

A. Target motion and measurement models

The target state vector $\boldsymbol{x}_k$ at time k is defined in Cartesian coordinates with the addition of the target's dimensions and orientation. Hence, we have:

$$\boldsymbol{x}_k \triangleq [x_k, \dot{x}_k, z_k, \dot{z}_k, l_k, w_k, \phi_k]^{\mathrm{T}} \tag{8}$$

where x_k, z_k and $\dot{x}_k$, $\dot{z}_k$ are the position and velocity components along the x, z directions, respectively, l_k and w_k represent the length and the width, respectively, ϕ_k is the orientation of the target. Note that usually ETT procedures assume that the target orientation is the same as the motion orientation, i.e. $\phi_k = \arctan(\dot{z}_k/\dot{x}_k)$. However in TWR tracking, this assumption seems to be not always true and, for this reason, target and motion orientations are assumed independent.

The motion of targets can be described with the nearly constant velocity model [28]. The target dynamic model is given by

$$\boldsymbol{x}_k = \mathbf{F}\ \boldsymbol{x}_{k-1} + \boldsymbol{\Gamma}\boldsymbol{w}_k \tag{9}$$

where

$$\mathbf{F} = \begin{bmatrix} \mathbf{I}_2 \otimes \widetilde{\mathbf{F}} & \mathbf{0}_{4\times 3} \\ \mathbf{0}_{3\times 4} & \mathbf{I}_3 \end{bmatrix}, \tag{10}$$

$$\boldsymbol{\Gamma} = \begin{bmatrix} \mathbf{I}_2 \otimes \widetilde{\boldsymbol{\Gamma}} & \mathbf{0}_{4\times 3} \\ \mathbf{0}_{3\times 2} & \mathbf{I}_3 \end{bmatrix}, \tag{11}$$

$$\widetilde{\mathbf{F}} = \begin{bmatrix} 1 & T_s \\ 0 & 1 \end{bmatrix}, \tag{12}$$

$\widetilde{\mathbf{\Gamma}} = [T_s^2/2,\ T_s]^{\mathrm{T}}$, $\mathbf{I}_d$ is the identity matrix with size d, $\mathbf{0}_{r\times c}$ represents the null matrix with r rows and c columns, T_s is the sampling time, $\otimes$ denotes the *Kronecker product*, and $\boldsymbol{w}_k$ takes into account the target acceleration and the unmodeled dynamics and it is assumed to be Gaussian with zero-mean and covariance matrix

$$\mathbf{Q} = \mathrm{diag}\left(\sigma_v^2, \sigma_v^2, \sigma_l^2, \sigma_w^2, \sigma_\phi^2\right), \tag{13}$$

where diag$(\cdot)$ denotes the diagonal matrix, and σ_v^2, σ_l^2, σ_w^2, and σ_ϕ^2 are the variances of the additive acceleration, length, width, and orientation, respectively.

The target originated measurement $\boldsymbol{\zeta}_k$ at frame k is given by

$$\boldsymbol{\zeta}_k = \mathbf{H}\boldsymbol{x}_k + \boldsymbol{n}_k \tag{14}$$

where

$$\mathbf{H} = \begin{bmatrix} \mathbf{I}_2 \otimes \widetilde{\mathbf{H}} & \mathbf{0}_{2\times 3} \\ \mathbf{0}_{3\times 4} & \mathbf{I}_3 \end{bmatrix}, \tag{15}$$

$\widetilde{\mathbf{H}} = [1,\ 0]$, and $\boldsymbol{n}_k$ is the measurement noise assumed to be Gaussian with zero-mean and covariance matrix

$$\mathbf{R} = \mathrm{diag}\left(\sigma_{n,x}^2, \sigma_{n,z}^2, \sigma_{n,l}^2, \sigma_{n,w}^2, \sigma_{n,\phi}^2\right) \tag{16}$$

where $\sigma_{n,x}^2$, $\sigma_{n,z}^2$ represent the variances along Cartesian axes, $\sigma_{n,l}^2$, $\sigma_{n,w}^2$ and $\sigma_{n,\phi}^2$ are the variances of sizes and orientation, respectively.

B. Multi-target tracking procedure

The tracking procedure is based on the JPDA paradigm, which is a Bayesian approach that associates all the validated measurements to the tracks by probabilistic weights. The track management is instead based on the popular M/N logic [28]. The filtering stage is performed using the Kalman filter (KF) [28]. We indicate with $\boldsymbol{x}_{k|k}^j$ ($\boldsymbol{x}_{k|k-1}^j$) and $\mathbf{P}_{k|k}^j$ ($\mathbf{P}_{k|k-1}^j$) the updated (predicted) target state and its covariance at time k, respectively.

Assume that, at frame k, a set of J_k tracks are active/preliminary $\mathcal{T}_k = \{\mathcal{T}_1(k), \mathcal{T}_2(k), \ldots, \mathcal{T}_{J_k}(k)\}$, where $\mathcal{T}_j(k)$ identifies the j^{th} track. A validation gate region $\mathcal{G}_k^j$, for all $j = \{1, 2, \ldots, J_k\}$, is constructed. Given that the target-originated measurements are Gaussian distributed around a predicted measurement $\boldsymbol{\zeta}_{k|k-1}^j = \mathbf{H}\boldsymbol{x}_{k|k-1}^j$ of target j, the gate is given by [28]

$$\mathcal{G}_k^j = \left\{ \boldsymbol{\zeta} : \left(\boldsymbol{\zeta} - \boldsymbol{\zeta}_{k|k-1}^j\right)^{\mathrm{T}} (\mathbf{S}_k^j)^{-1} \left(\boldsymbol{\zeta} - \boldsymbol{\zeta}_{k|k-1}^j\right) < \gamma \right\} \tag{17}$$

where $\mathbf{S}_k^j = \mathbf{H}\,\mathbf{P}_{k|k-1}^j\mathbf{H}^{\mathrm{T}} + \mathbf{R}$ is the innovation covariance, while the threshold γ determines the gating probability P_G, which is the probability that a measurement originated by target j is correctly validated.

The track management is divided into the following steps.

Track initiation: A measurement is associated to the track $\mathcal{T}_j(k)$ if it falls in its gate region. Every unassociated measurement is called *initiator* and yields a *tentative track*. Following the detection of an initiator, a gate is set up. If a detection falls in the gate, this track becomes a *preliminary track*; otherwise, it is dropped. For each preliminary track, the JPDA can be initialized and used to set up a gate for the next sampling time. Starting from the third scan, a logic of M detections out of N scans is used for the subsequent gates. If, at the end (scan N + 2), the logic requirement is satisfied, the track becomes a *confirmed* or *active track*; otherwise, it is discarded.

Track termination: A confirmed track is terminated if one of the following conditions is verified: 1) No detection has been validated in the past N^* most recent sampling times; 2) The target's track uncertainty, evaluated from its covariance matrix, has grown beyond a given threshold; 3) The target has reached an unfeasible maximum velocity v_{max}.

Track update: For each active and preliminary track, the target state is updated applying the JPDA rule [28], [52].

The target state is updated according to the measurement-to-track association rule of the JPDA, while the target state prediction follows directly from the motion model.

Data association: A validation matrix is set up for all the confirmed and preliminary targets. This matrix is populated with all the validated measurements falling in the gate, plus the case of no measurement. All the feasible joint association events are constructed in the following way. Each measurement is originated from one target or it is a false alarm. Each target generates, at most, one measurement, with detection probability P_D.

The probabilities of the joint events are evaluated assuming that: 1) Target-originated measurements are Gaussian distributed around the predicted location of the corresponding target measurement; 2) False alarms are distributed in the surveillance region according to a Poisson point process of parameter λ, which represents the clutter density, assumed uniformly distributed in the gating region. The marginal association probabilities of target j with measurement i, $\beta_{i,k}^j$, are obtained by summing over all the joint events in which the marginal event of interest occurs (see [28], [30] for further details).

Update and prediction: The j^{th} target state $\boldsymbol{x}_{k|k}^j$ and its covariance $\mathbf{P}_{k|k}^j$ are then updated by averaging the updates for all the validated measurements with the association probabilities [28]

$$\boldsymbol{x}_{k|k}^j = \boldsymbol{x}_{k|k-1}^j + \mathbf{K}_k^j \boldsymbol{v}_k^j, \tag{18}$$

$$\begin{aligned} \mathbf{P}_{k|k}^j = \mathbf{P}_{k|k-1}^j - \left(\sum_{i=1}^{m_k^j} \beta_{i,k}^j\right) \mathbf{K}_k^j \mathbf{S}_k^j \left(\mathbf{K}_k^j\right)^{\mathrm{T}} \\ + \mathbf{K}_k^j \left(\sum_{i=1}^{m_k^j} \beta_{i,k}^j \boldsymbol{v}_{i,k}^j \left(\boldsymbol{v}_{i,k}^j\right)^{\mathrm{T}} - \boldsymbol{v}_k^j \left(\boldsymbol{v}_k^j\right)^{\mathrm{T}}\right) \left(\mathbf{K}_k^j\right)^{\mathrm{T}}, \end{aligned} \tag{19}$$

where $\boldsymbol{v}_k^j = \sum_{i=1}^{m_k^j} \beta_{i,k}^j \boldsymbol{v}_{i,k}^j$ is the combined innovation, $\boldsymbol{v}_{i,k}^j = \boldsymbol{\zeta}_{i,k}^j - \boldsymbol{\zeta}_{k|k-1}^j$ is the innovation for the i^{th} validated measurement, $\mathbf{K}_k^j = \mathbf{P}_{k|k-1}^j \mathbf{H}^{\mathrm{T}} \left(\mathbf{S}_k^j\right)^{-1}$ is the Kalman gain, m_k^j is the number of validated measurements, and $\boldsymbol{\zeta}_{i,k}^j$ is the i^{th} validated measurement.

The predicted state $\boldsymbol{x}_{k+1|k}^j$ and its covariance $\mathbf{P}_{k+1|k}^j$ are obtained by the standard KF prediction step.

V. Numerical tests

In this Section, numerical tests based on synthetic data are reported to validate the proposed TWR signal processing chain in Fig. 2. The TWR signals are generated for the indoor scenario depicted in Fig. 3 by using a finite-difference time-domain forward solver. The room walls are made of concrete with relative permittivity $\epsilon_w = 4$ and conductivity $\sigma_w = 0.01$ S/m. The external walls have thickness $t = 0.3$ m and the inner dimensions of the room are $L_x = L_z = 4$ m. Two internal walls with length 1 m and thickness 0.15m are present in the room at a distance of 2m from the front wall. Moreover, a static dielectric object (size $0.2\text{m}\times1\text{m}$) resembling a piece of furniture and having relative permittivity equal to 6 is placed nearby the right perimetral wall. The scene is probed by an array with length $L = 3$ m which is placed at a distance of $h = 0.5$ m from the front wall. Each antenna radiates a Ricker wavelet with central frequency of 1.5 GHz and collects the radar echo over the fast-time window $[0, 40.0]$ ns. The spacing between radiating elements is uniform and fixed to 0.1m.

In order to perform the imaging task, the region D corresponding to the room is discretized into square pixels with size 0.05 m. A pre-processing step consisting of a time gating of the radar signal falling in the fast-time window $[0, 10]$ ns is performed to the filter out both the direct coupling and the main front wall echoes. the remaining signals are transformed into frequency domain. In particular, the frequency interval $[1.0, 2.0]$ GHz discretized with a step of 0.025 GHz is considered for the inversion. The frequency domain scattered field data are then corrupted with Additive White Gaussian Noise (AWGN) by assuming a signal-to-noise ratio equal to 10 dB.

Each dataset is recorded and processed to form a tomographic image every 0.1s (i.e. frame rate 10 Hz). Such a value is realistic and compatible with current hardware implementations of TWRs [53]. The slow-time observation window $[0, 5]$ s corresponding to a sequence of 51 images is considered for the application of the ETT procedure.

The OS-CFAR detector has been set by considering a P_{FA} = 1e-5 and the 75^{th} percentile for the threshold evaluation. In addition, the reference window has been fixed to 13×13 pixels, and a guard window of 7×7 pixels has proved to be a good choice in view of the TWR resolution and size of practical targets. As regards to the tracker parameters, they are summarized in Tab. I.

The first numerical test-bed refers to a single target scenario as shown in Fig. 3. The target is a metallic cylinder with radius 0.15 m resembling a human. Its center moves from $(1.3, 0.9)$ m to $(1.0, 3.9)$ m according to a uniform circular motion. The velocity along the trajectory is kept constant to 1.0 m/s.

As an example for reader's convenience, Fig. 4 displays the time domain TWR raw data collected along the array at $t_s = 0$ after the application of the time gating procedure. The black arrows indicate the visible radar signatures. As can be seen, these are associated with the metallic cylinder, the two walls in the center of the room and the back wall.

Figure 5 shows the tomographic images corresponding to the datasets collected at $t_s = 0, 1, 2, 3, 4, 5$ s, respectively. It can be seen that a spot always appears corresponding to the upper edge of the cylinder. Actually, the correct localization is made possible since the propagation through the front wall has been properly compensated [9]. In addition to the true target, minor intensity spots appears in correspondence of the internal walls. The weaker response is due to the lower reflectivity walls with respect to the target.

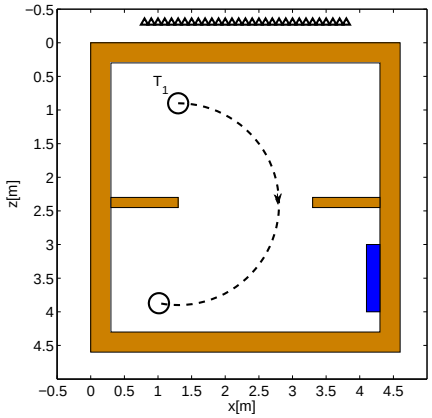

Fig. 3. Single-target TW scenario. The dashed line depicts the true trajectory.

TABLE I
Parameter Settings for the JPDA Tracker

Parameter	Value	Specification
T_s	0.1 s	Sampling time
σ_v	0.9 m s^{-2}	Process noise
σ_l	0.001 m	Process noise
σ_w	0.001 m	Process noise
σ_ϕ	$\pi/24$ rad	Process noise
$\sigma_{n,x}$	0.02 m	Std. dev. x
$\sigma_{n,z}$	0.02 m	Std. dev. z
$\sigma_{n,l}$	0.05 m	Std. dev. length
$\sigma_{n,w}$	0.05 m	Std. dev. width
$\sigma_{n,\phi}$	$\pi/3$ rad	Std. dev. orientation
P_D	0.9	Detection probability
P_G	1	Gate probability
λ	10^{-5} m^{-2}	Clutter density
γ	5^2	Gate threshold
v_{max}	5 m s^{-1}	Maximum velocity
M/N	$5/6$	Track initialization logic
M^*/N^*	$8/8$	Track termination logic

The clustered detections corresponding to the images in Fig. 5 are illustrated in Fig. 6. Some important remarks are in order. First, the target is always detected save for the final dataset (see last panel of Fig. 6). This is attributed to the selected value of P_{FA} which allows, on one hand, suppression of internal walls, but the true target, on the other hand, is missed. This occurred as the level of surrounding clutter assumes comparable response when target is placed behind the left interior wall (see last panel of Fig. 5). As will be later shown, this does represent a serious problem since the target can be identified at the tracking stage.

In Fig. 7, the outputs of the ETT procedure (dotted lines) are compared to the true target state (solid lines). In particular, the top panels refer to the target position along x (left) and z (right). The middle panels compare the estimated and true velocities of the target along x (left) and z (right). The bottom panels are concerned with the estimated length (left) and width

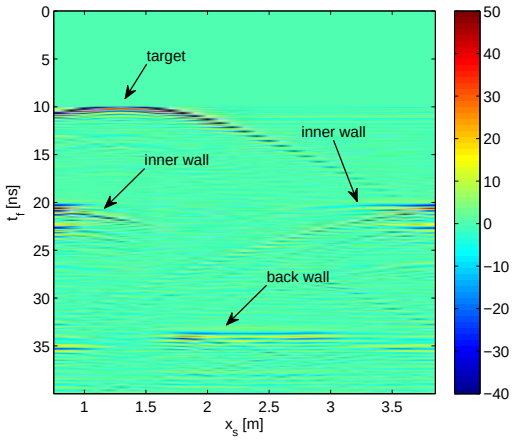

Fig. 4. TWR signal after the time gating procedure for dataset at $t_s = 0$ s. Single-target case. The arrows are associated to the visible radar signatures.

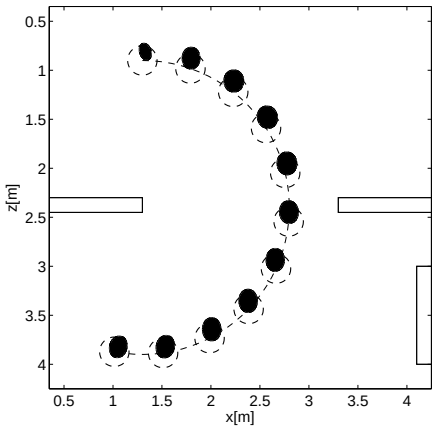

Fig. 8. Estimated vs true track in single-target case. The reference trajectory and true object are represented with dashed lines. The ellipses modeling the target are superimposed to the true object. The tracking results are decimated by a factor 5 to improve readability.

(right) of the ellipses modeling the target shape. It can be seen that an excellent agreement between the estimated and true values is generally reached. However, the estimated position along z is characterized by an almost constant offset with respect to the true position. The physical justification of this phenomenon resides in the fact that the TWR allows imaging only the upper edge of the object. On the other hand, the true position is evaluated by considering the center of the target. Nevertheless, it is reasonable to assume that this kind of offset can be tolerated in real TWR applications.

It must be also noticed that the estimated sizes of the ellipse (bottom panels) and their orientations (see Fig. 8) vary along the trajectory depending on how the target is seen by the radar. Most notably, they always underestimate the true target dimensions because only the upper part of the object is imaged. This claim is further elucidated by the results illustrated in Fig. 8, where the estimated ellipses are compared to the true object along the trajectory. As can be seen, the sizes of the ellipse provide useful information but do not accurately reveal the target extent. This is still preferred compared to tracking approaches based on Kalman filter which track only a point [21]–[23].

The next test-bed is concerned with the multi-target TW scenario depicted in Fig. 9. The geometrical and electrical properties of the layout are those considered in the previous example. Three metallic cylinders (T_1, T_2, T_3) having different sizes are simultaneously moving in the room. T_1 is the target of previous example and follows the same trajectory. T_2 has radius 0.225 m and moves from $(0.8, 4.0)$ m to $(2.9, 1.9)$ m following a linear trajectory with constant speed of 0.6 m/s. T_3 has radius 0.187 m and moves from $(3.7, 4.0)$ m to $(0.5, 0.8)$ m along a line with constant speed of 0.9 m/s. As depicted in Fig. 9, the targets become in the same vicinity as they approach the center of the room which represents a useful scenario to test the performance of the ETT procedure. In this case, target-to-target interactions are expected to produce ghost objects at locations where no physical target exists, with a consequent increase in the number of false alarms [54].

The TW images obtained from data recorded at $t_s =$

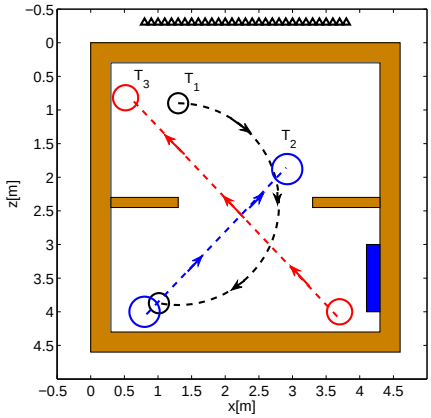

Fig. 9. Multi-target TW scenario. The dashed lines depicts the true tracks. Different colors are used to indicate the targets: T_1 (black), T_2 (blue), T_3 (red).

$0, 1, 2, 3, 4, 5$ s are reported in Fig. 10. From such figures, it emerges that the targets are always correctly localized, but they are imaged as spots of variable intensity depending on their downrange (e.g. see images at $t_s = 0, 1, 4, 5$ s). This is a peculiar feature of adjoint inversion which can be easily explained by considering the SVD expansion [48]. Furthermore, as stated before, the images corresponding to $t_s = 2, 3$ s confirm the presence of some spurious targets among true objects.

Figure 11 displays the outputs of the ETT procedure and the targets are reasonably tracked. Interestingly, the tracks relevant to T_2 and T_3 require some time (respectively 1.2s and 0.7s) to be initialized. Indeed, in agreement with data in Fig. 10, T_2 and T_3 produce a weak response in the interval $[0, 1]$s because they are partly hidden by the internal walls. Therefore they are not visible at the detector output. Once the three tracks are formed, the system is capable to follow all targets even when they are close each other, and the false alarms related to ghost targets are effectively filtered out. In the time interval $[3.6, 4.5]$ s, the target T_1 is out of the true track

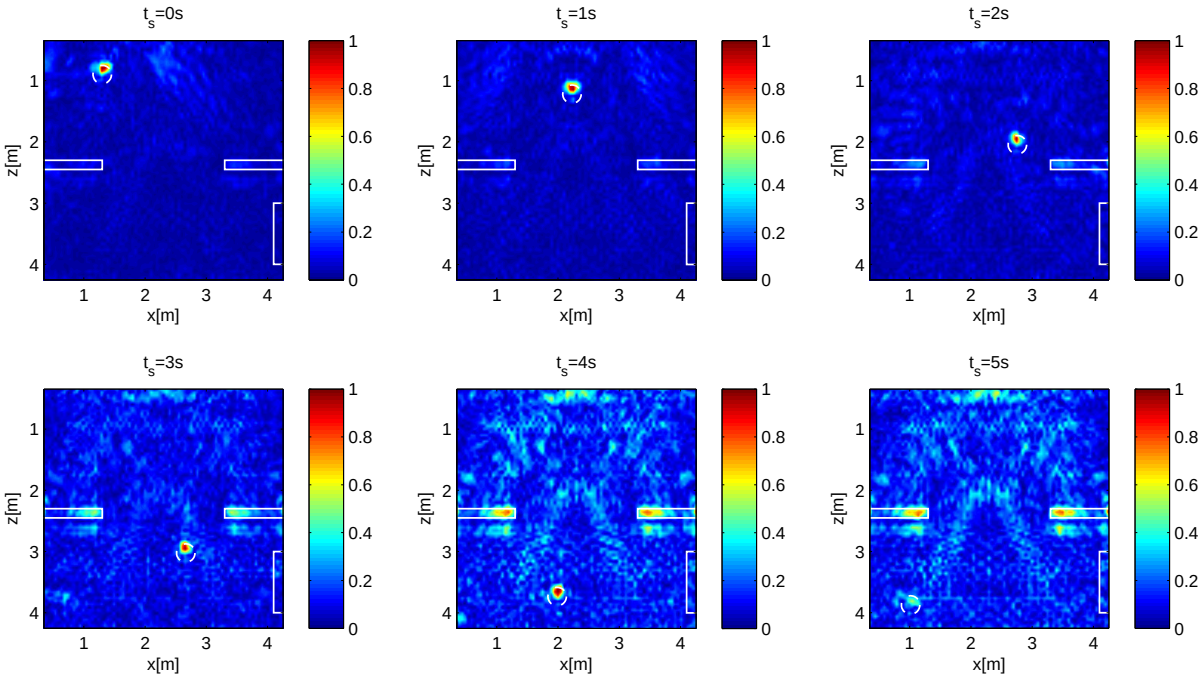

Fig. 5. Tomographic images of data frames recorded at $t_s = 0, 1, 2, 3, 4, 5$ s in the single target case. The white lines depict the ground truth.

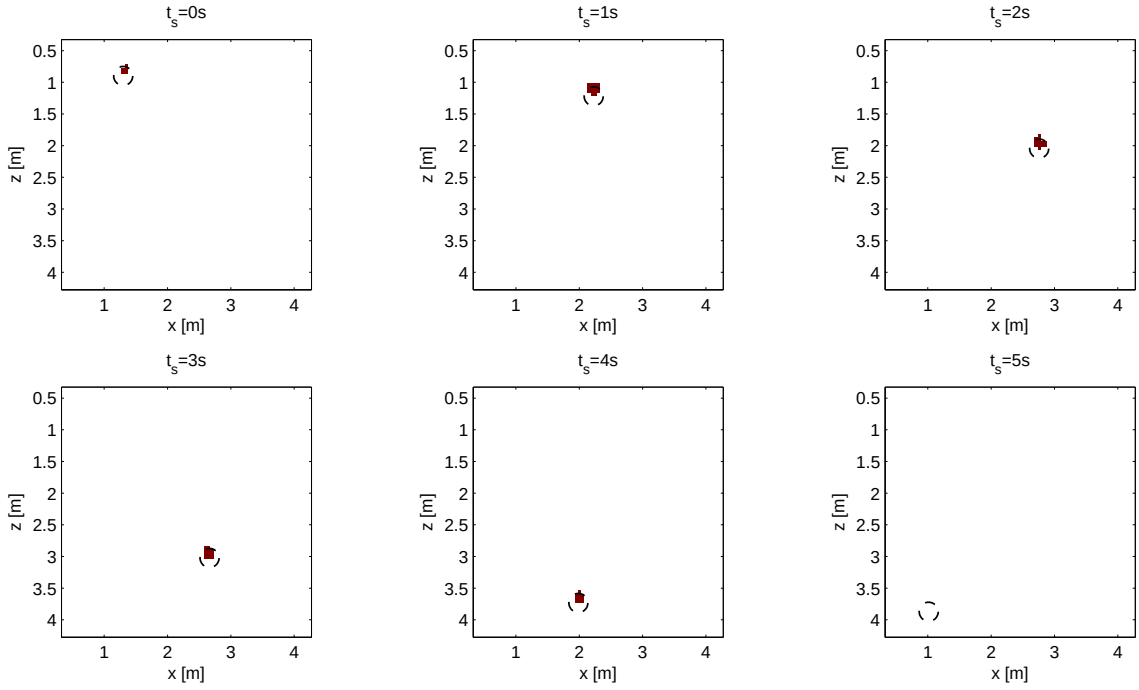

Fig. 6. Detection outputs of data frames recorded at $t_s = 0, 1, 2, 3, 4, 5$ s in the single target case. The white lines depict the ground truth.

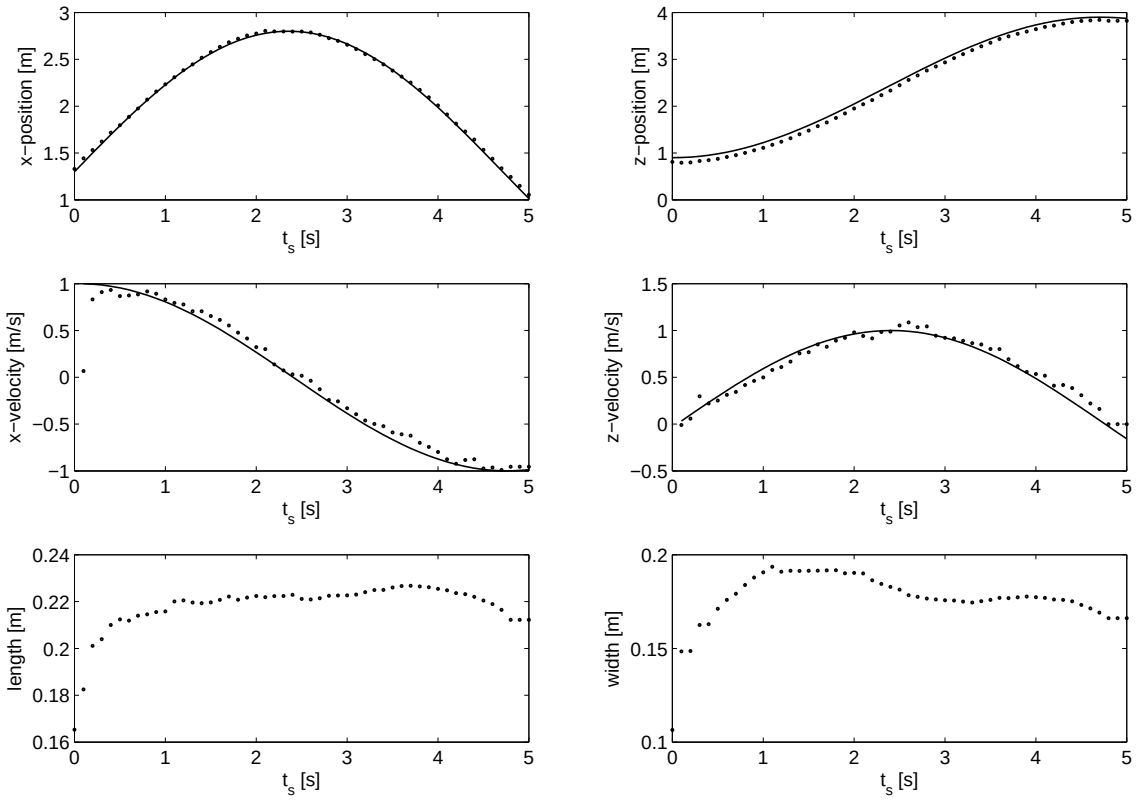

Fig. 7. Output of the ETT procedure (markers) in single target case. The solid lines represent the ground truth.

(see top left panel of Fig. 11) because it is not detectable due to the shadowing caused by the biggest target T_2. Note that, as before, an offset along z is present when comparing the estimated position to the ground truth. As for the estimated velocities, the comparisons follow the same aforementioned limitations. The same behavior encountered in the single-target case holds true for the estimated sizes of the objects, as confirmed by the results shown in Fig. 12.

Finally, in order to provide a quantitative assessment of the tracking performance, the following metrics, introduced in [52], are adopted:

- The normalized time-on-target (ToT) is defined as the ratio between the estimated and the real track length. Its ideal value is 1, which can be reached when the tracker is able to properly follow the target in the scenario under test;
- The false alarm rate (FAR) is defined as the number of false track contacts, normalized with the recording interval and the area of the surveyed region. Its ideal value is 0 corresponding to the case of no false alarm;
- The errors committed by the tracker are also evaluated. The tracker accuracy is thus defined in position (i.e. $\epsilon^{(p)}$), velocity (i.e. $\epsilon^{(v)}$), width (i.e. $\epsilon^{(w)}$), length (i.e. $\epsilon^{(l)}$), and orientation (i.e. $\epsilon^{(\phi)}$).

The association procedure between the estimated tracks and the ground-truth is performed by exploiting a nearest neighbor logic. A first analysis is performed by comparing the ToT and the FAR with and without the introduction of the JPDA tracker. The outcomes are summarized in Tab. II. An improvement in both indexes, due to the introduction of the tracker, is evident. The maximum increase of the ToT (about 25%) is observed for the track T_1 on the *multi-target case* dataset. This can be mainly justified by the fact that this target is often shadowed by either other targets or internal walls. Thus, the tracker's action in aiding the track maintenance is more evident in this case. Generally speaking, the average ToT% is about 90% (about 10% greater than the one based on the sole object detection) with two targets perfectly tracked when the overall signal processing chain is adopted, which points out the ability of the tracker to follow targets in several conditions. Regarding the FAR index, ideal values (i.e. no false alarm is detected) are obtained for each test case when the tracker is exploited, while, a false alarm rate appreciably different from 0 is present when the sole object detection phase is employed. This result corroborates the ability of the tracker to properly filter out the clutter coming from the detection step. The last analysis exploits the tracker accuracy metrics. Good outcomes are also obtained in this case. They are summarized in Tab. III. The errors in position stem from the fact that we are able to track only the part of targets that scatter in the scene and, therefore, some biases between the real and the estimated target positions can be found. For the same reason, the considerable errors in the size estimation can be justified.

VI. Conclusion

In this paper, a signal processing approach has been proposed for tracking multiple extended targets by a TWR. It consists of a pre-processing of raw data, model-based image

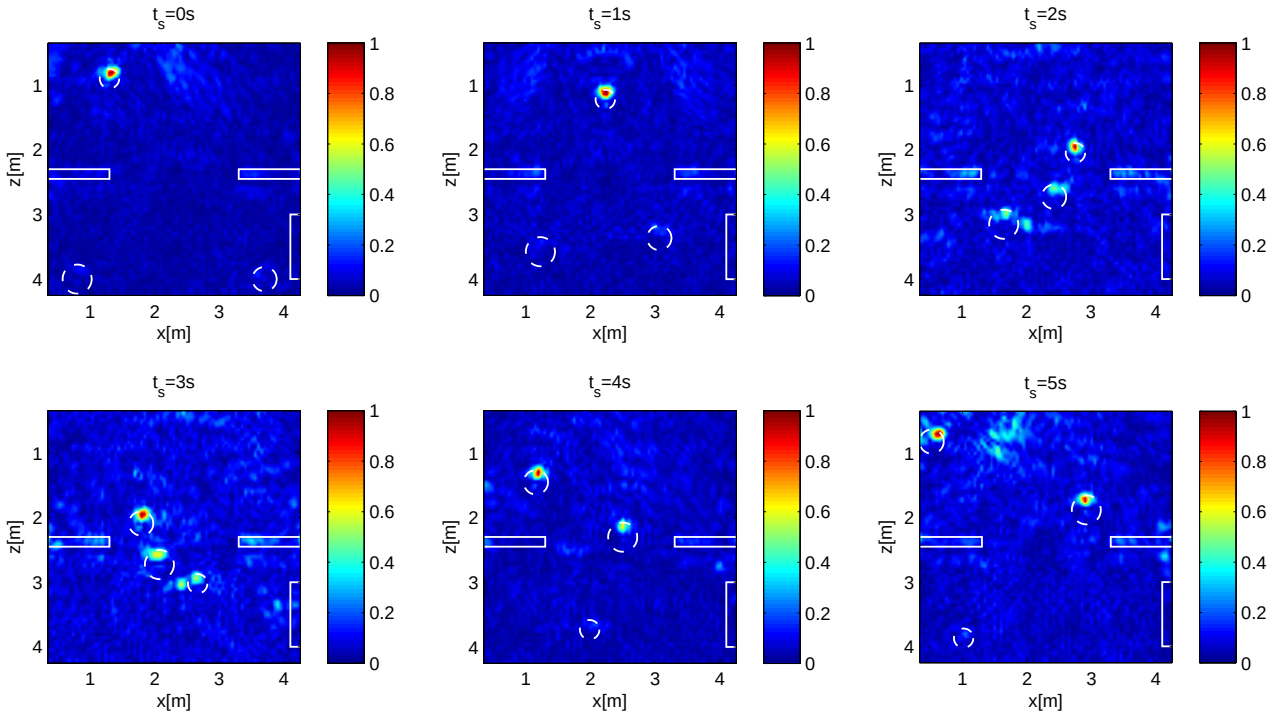

Fig. 10. Tomographic images of data frames at $t_s = 0, 1, 2, 3, 4, 5$ s. Multi-target case. The white lines depict the ground truth.

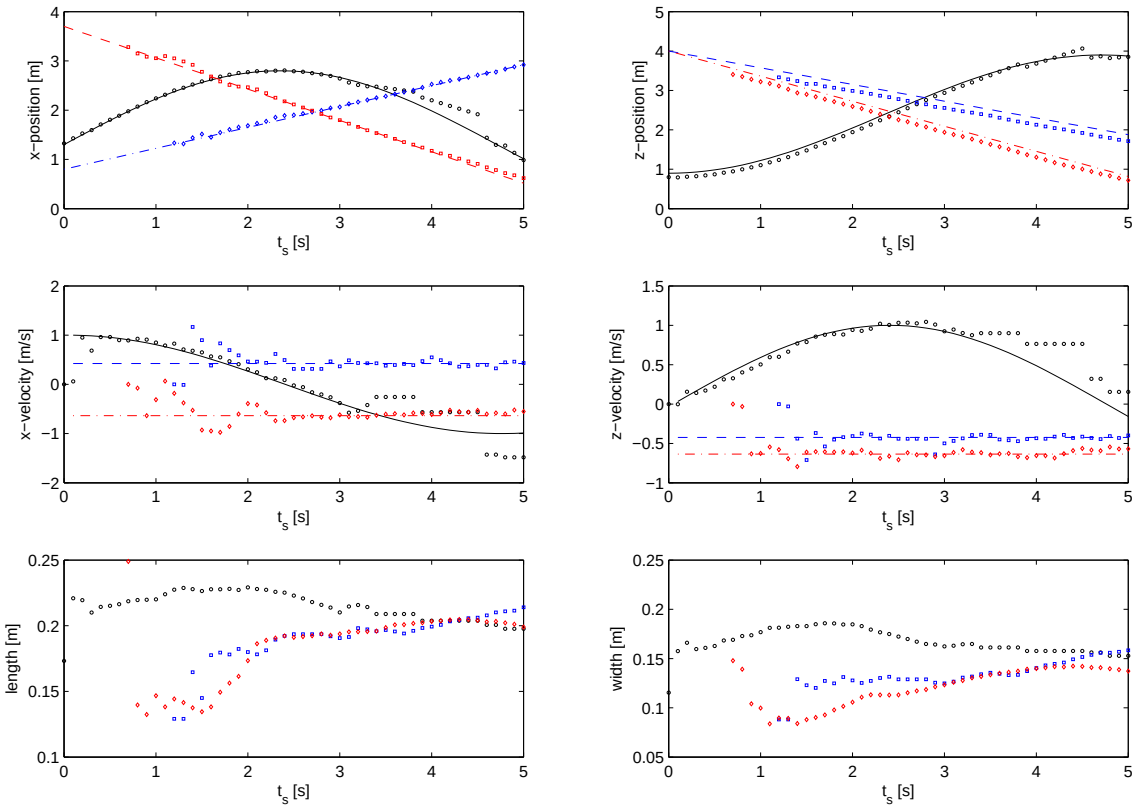

Fig. 11. Results of the ETT procedure (markers) in multi-target case. The lines represent the ground truth and different colors are used to indicate the targets: T_1 (black), T_2 (blue), T_3 (red).

TABLE II
TOT AND FAR FOR BOTH OBJECT DETECTION AND OBJECT DETECTION + JPDA ON THE TWO DATASETS

Dataset	Id Track	Object Detection			Object Detection + JPDA		
		ToT%	Average ToT%	FAR $[s^{-1}m^{-2}]$	ToT%	Average ToT%	FAR $[s^{-1}m^{-2}]$
single-target case	T_1	94.12	94.12	$3.8 \cdot 10^{-1}$	100.0	100.0	0
multi-target case	T_1	74.51	77.13	$6.5 \cdot 10^{-1}$	100.0	87.58	0
	T_2	68.63			72.55		
	T_3	88.24			90.20		

TABLE III
JPDA TRACKER ACCURACY FOR THE TWO DATASETS

Dataset	Id Track	$\epsilon^{(p)}$ [m]	$\epsilon^{(v)}$ $[ms^{-1}]$	$\epsilon^{(l)}$ [m]	$\epsilon^{(w)}$ [m]	$\epsilon^{(\phi)}$ [rad]
single-target case	T_1	0.0949	0.1413	0.1004	0.0512	0.0693
multi-target case	T_1	0.1007	0.2307	0.1073	0.0642	0.1114
	T_2	0.1669	0.1216	0.3317	0.2701	0.1355
	T_3	0.1460	0.1504	0.2723	0.2373	0.0330

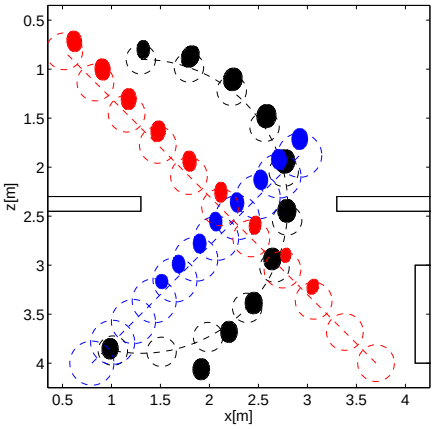

Fig. 12. Estimated vs true tracks in multi-target case. The reference trajectories and true objects are represented with dashed lines. The ellipses modeling the targets are superimposed to the true objects. The tracking results are decimated by a factor 5 to improve readability. Different colors are used to indicate the targets: T_1 (black), T_2 (blue), T_3 (red).

formation, object detection, and tracking. The extended target tracking paradigm has been introduced to account for the distributed nature of targets. Indeed, several detections are available per object and this additional information is conveniently exploited during the tracking stage. As a byproduct, besides targets' dynamics, the tracker provides a rough estimation of their sizes, which are underestimated due to the underlying physical constraints of the TW imaging system. A comprehensive analysis has been carried out to analyze in detail the various steps of the proposed signal processing via numerical simulations pertaining to a complex indoor scenario. An assessment of tracking performance was made in both single-target and multi-target cases. While track estimation errors are very low in the single target scenario, multi-target tracking is a more challenging because of shadowing and mutual interactions among targets. The results of this study are very promising and suggest the application of the proposed approach for multi-target tracking in realistic three-dimensional environments.

REFERENCES

[1] E. J. Baranoski, "Through-wall imaging: Historical perspective and future directions," *Journal of the Franklin Institute*, vol. 345, no. 6, pp. 556–569, 2008.

[2] M. G. Amin, *Through-the-wall radar imaging*. CRC press, 2011.

[3] Y.-S. Yoon and M. G. Amin, "Spatial filtering for wall-clutter mitigation in through-the-wall radar imaging," *IEEE Transactions on Geoscience and Remote Sensing*, vol. 47, no. 9, pp. 3192–3208, 2009.

[4] F. Tivive, A. Bouzerdoum, and M. Amin, "A subspace projection approach for wall clutter mitigation in through-the-wall radar imaging," *IEEE Transactions on Geoscience and Remote Sensing*, vol. 53, no. 4, pp. 2108–2122, April 2015.

[5] F. Ahmad, Y. Zhang, and M. G. Amin, "Three-dimensional wideband beamforming for imaging through a single wall," *IEEE Geoscience and Remote Sensing Letters*, vol. 5, no. 2, pp. 176–179, 2008.

[6] W. Zhang, A. Hoorfar, and L. Li, "Through-the-wall target localization with Time Reversal Music method," *Progress In Electromagnetics Research*, vol. 106, pp. 75–89, 2010.

[7] L.-P. Song, C. Yu, and Q. H. Liu, "Through-wall imaging (twi) by radar: 2-d tomographic results and analyses," *IEEE Transactions on Geoscience and Remote Sensing*, vol. 43, no. 12, pp. 2793–2798, 2005.

[8] W. Zhang and A. Hoorfar, "Three-dimensional real-time through-the-wall radar imaging with diffraction tomographic algorithm," *IEEE Transactions on Geoscience and Remote Sensing*, vol. 51, no. 7, pp. 4155–4163, 2013.

[9] F. Soldovieri and R. Solimene, "Through-wall imaging via a linear inverse scattering algorithm," *IEEE Geoscience and Remote Sensing Letters*, vol. 4, no. 4, pp. 513–517, 2007.

[10] R. Solimene, F. Soldovieri, G. Prisco, and R. Pierri, "Three-dimensional through-wall imaging under ambiguous wall parameters," *IEEE Transactions on Geoscience and Remote Sensing*, vol. 47, no. 5, pp. 1310–1317, 2009.

[11] M. Dehmollaian and K. Sarabandi, "Refocusing through building walls using synthetic aperture radar," *IEEE Transactions on Geoscience and Remote Sensing*, vol. 46, no. 6, pp. 1589–1599, 2008.

[12] G. Gennarelli and F. Soldovieri, "Radar imaging through cinderblock walls: Achievable performance by a model-corrected linear inverse scattering approach," *IEEE Transactions on Geoscience and Remote Sensing*, vol. 52, no. 10, pp. 6738–6749, 2014.

[13] P. Setlur, M. Amin, and F. Ahmad, "Multipath model and exploitation in through-the-wall and urban radar sensing," *IEEE Transactions on Geoscience and Remote Sensing*, vol. 49, no. 10, pp. 4021–4034, Oct 2011.

[14] G. Gennarelli, G. Riccio, R. Solimene, and F. Soldovieri, "Radar imaging through a building corner," *IEEE Transactions on Geoscience and Remote Sensing*, vol. 52, no. 10, pp. 6750–6761, 2014.

[15] M. Leigsnering, M. G. Amin, F. Ahmad, and A. M. Zoubir, "Multipath exploitation and suppression for sar imaging of building interiors," *IEEE Signal Processing Magazine*, vol. 31, no. 4, pp. 110–119, 2014.

[16] R. Solimene, I. Catapano, G. Gennarelli, A. Cuccaro, A. Dell'Aversano, and F. Soldovieri, "Sar imaging algorithms and some unconventional applications," *IEEE Signal Processing Magazine*, vol. 31, no. 4, pp. 90–98, 2014.

[17] C. Debes, M. G. Amin, and A. M. Zoubir, "Target detection in single- and multiple-view through-the-wall radar imaging," *IEEE Transactions on Geoscience and Remote Sensing*, vol. 47, no. 5, pp. 1349–1361, 2009.

[18] C. Debes, J. Riedler, A. M. Zoubir, and M. G. Amin, "Adaptive target detection with application to through-the-wall radar imaging," *IEEE Transactions on Signal Processing*, vol. 58, no. 11, pp. 5572–5583, 2010.

[19] C. Debes, J. Hahn, A. M. Zoubir, and M. G. Amin, "Target discrimination and classification in through-the-wall radar imaging," *IEEE Transactions on Signal Processing*, vol. 59, no. 10, pp. 4664–4676, 2011.

[20] G. E. Smith and B. G. Mobasseri, "Robust through-the-wall radar image classification using a target-model alignment procedure," *IEEE Transactions on Image Processing*, vol. 21, no. 2, pp. 754–767, 2012.

[21] R. Jana and D. Kocur, "Compensation of wall effect for through wall tracking of moving targets," *Radioengineering*, vol. 18, no. 2, p. 189, 2009.

[22] Y. He, T. Savelyev, and A. Yarovoy, "Two-stage algorithm for extended target tracking by multistatic UWB radar," in *International Conference on Radar*, vol. 1, 2011, pp. 795–799.

[23] X. Chen, H. Leung, and M. Tian, "Multitarget detection and tracking for through-the-wall radars," *IEEE Transactions on Aerospace and Electronic Systems*, vol. 50, no. 2, pp. 1403–1415, 2014.

[24] M. G. Amin and F. Ahmad, "Change detection analysis of humans moving behind walls," *IEEE Transactions on Aerospace and Electronic Systems*, vol. 49, no. 3, pp. 1410–1425, 2013.

[25] F. Ahmad and M. G. Amin, "Through-the-wall human motion indication using sparsity-driven change detection," *IEEE Transactions on Geoscience and Remote Sensing*, vol. 51, no. 2, pp. 881–890, 2013.

[26] G. Gennarelli, I. Catapano, and F. Soldovieri, "Rf/microwave imaging of sparse targets in urban areas," *IEEE Antennas and Wireless Propagation Letters*, vol. 12, pp. 643–646, 2013.

[27] A. F. Martone, K. Ranney, and C. Le, "Noncoherent approach for through-the-wall moving target indication," *IEEE Transactions on Aerospace and Electronic Systems*, vol. 50, no. 1, pp. 193–206, 2014.

[28] Y. Bar-Shalom, P. Willett, and X. Tian, *Tracking and Data Fusion: A Handbook of Algorithms*. Storrs, CT: YBS Publishing, 2011.

[29] R. Mahler, *Statistical Multisource-Multitarget Information Fusion*. Artech House, 2007.

[30] Y. Bar-Shalom, F. Daum, and J. Huang, "The probabilistic data association filter," *IEEE Control Syst. Mag.*, vol. 29, no. 6, pp. 82–100, Dec. 2009.

[31] O. Cappe, S. Godsill, and E. Moulines, "An overview of existing methods and recent advances in sequential Monte Carlo," *Proc. IEEE*, vol. 95, no. 5, pp. 899–924, 2007.

[32] P. Braca, P. Willett, K. LePage, S. Marano, and V. Matta, "Bayesian tracking in underwater wireless sensor networks with port-starboard ambiguity," *IEEE Trans. Signal Process.*, vol. 62, no. 7, pp. 1864–1878, Apr. 2014.

[33] P. Braca, R. Goldhahn, K. LePage, P. Willett, S. Marano, and V. Matta, "Cognitive multistatic auv networks," in *Proc. of the* 17^{th} *Intern. Conf. on Inform. Fusion (FUSION)*, Salamanca, 2014.

[34] B.-T. Vo, B.-N. Vo, and A. Cantoni, "Bayesian filtering with random finite set observations," *IEEE Trans. Signal Process.*, vol. 56, no. 4, pp. 1313–1326, Apr. 2008.

[35] P. Braca, S. Marano, V. Matta, and P. Willett, "Asymptotic efficiency of the PHD in multitarget/multisensor estimation," *IEEE J. Sel. Topics Signal Process.*, vol. 7, no. 3, pp. 553–564, 2013.

[36] O. E. Drummond, S. S. Blackman, and G. C. Pretrisor, "Tracking clusters and extended objects with multiple sensors," in *Proc. SPIE*, 1990, pp. 362–375.

[37] B. Errasti-Alcala and P. Braca, "Track before detect algorithm for tracking extended targets applied to real-world data of x-band marine radar," in *Proceedings of the International Conference on Information Fusion*, Salamanca, Spain, Jul. 2014.

[38] K. Granström, A. Natale, P. Braca, G. Ludeno, and F. Serafino, "PHD Extended Target Tracking Using an Incoherent X-band Radar: Preliminary Real-World Experimental Results," in *Proceedings of the International Conference on Information Fusion*, Salamanca, Spain, Jul. 2014.

[39] S. Davey, M. Wieneke, and H. Vu, "Histogram-PMHT unfettered," *IEEE Journal of Selected Topics in Signal Processing*, vol. 7, no. 3, pp. 435–447, June 2013.

[40] K. Granström, C. Lundquist, and U. Orguner, "Extended Target Tracking using a Gaussian Mixture PHD filter," *IEEE Transactions on Aerospace and Electronic Systems*, vol. 48, no. 4, pp. 3268–3286, Oct. 2012.

[41] J. W. Koch, "Bayesian approach to extended object and cluster tracking using random matrices," *IEEE Transactions on Aerospace and Electronic Systems*, vol. 44, no. 3, pp. 1042–1059, Jul. 2008.

[42] Y. Boers, H. Driessen, J. Torstensson, M. Trieb, R. Karlsson, and F. Gustafsson, "A track before detect algorithm for tracking extended targets," *IEE Proceedings Radar, Sonar and Navigation*, vol. 153, no. 4, pp. 345–351, Aug. 2006.

[43] H. Rohling, "Radar CFAR thresholding in clutter and multiple target situations," *IEEE Transactions on Aerospace and Electronic Systems*, vol. AES-19, no. 4, pp. 608–621, July 1983.

[44] W. C. Chew, *Waves and fields in inhomogeneous media*. IEEE press New York, 1995, vol. 522.

[45] R. Pierri, A. Liseno, R. Solimene, and F. Soldovieri, "Beyond physical optics svd shape reconstruction of metallic cylinders," *IEEE Transactions on Antennas Propagation*, vol. 54, no. 2, pp. 655–665, 2006.

[46] G. Gennarelli and F. Soldovieri, "A linear inverse scattering algorithm for radar imaging in multipath environments," *IEEE Geoscience and Remote Sensing Letters*, vol. 10, pp. 1085–1089, 2013.

[47] G. Gennarelli, M. Amin, F. Soldovieri, and R. Solimene, "Passive multiarray image fusion for rf tomography by opportunistic sources," *IEEE Geoscience and Remote Sensing Letters*, vol. 12, no. 3, pp. 641–645, 2015.

[48] M. Bertero and P. Boccacci, *Introduction to inverse problems in imaging*. CRC press, 1998.

[49] M. Feldmann, D. Fränken, and J. W. Koch, "Tracking of extended objects and group targets using random matrices," *IEEE Transactions on Signal Processing*, vol. 59, no. 4, pp. 1409–1420, Apr. 2011.

[50] K. Granström and U. Orguner, "A PHD filter for tracking multiple extended targets using random matrices," *IEEE Transactions on Signal Processing*, vol. 60, no. 11, pp. 5657–5671, Nov. 2012.

[51] R. M. Haralick and L. G. Shapiro, *Computer and Robot Vision*. Addison-Wesley Longman Publishing Co., Inc. Boston, MA, USA, 1992.

[52] S. Maresca, P. Braca, J. Horstmann, and R. Grasso, "Maritime surveillance using multiple high-frequency surface-wave radars," *IEEE Trans. Geosci. Remote Sens.*, vol. 52, no. 8, pp. 5056–5071, Aug. 2014.

[53] T. Ralston, G. Charvat, and J. Peabody, "Real-time through-wall imaging using an ultrawideband multiple-input multiple-output (mimo) phased array radar system," in *IEEE International Symposium on Phased Array Systems and Technology (ARRAY)*, 2010, pp. 551–558.

[54] G. Gennarelli and F. Soldovieri, "Multipath ghosts in radar imaging: Physical insight and mitigation strategies," *IEEE Journal of Selected Topics in Applied Earth Observations and Remote Sensing*, vol. PP, no. 99, pp. 1–9, 2014.